

Supplemental Data

Entrainment of Neocortical Neurons and Gamma Oscillations

by the Hippocampal Theta Rhythm

Anton Sirota, Sean Montgomery, Shigeyoshi Fujisawa, Yoshikazu Isomura, Michael Zugaro, and György Buzsáki

Supplemental Experimental Procedures

Chronic Animal Surgery

For chronic experiments, 28 Long Evans rats (male, 250-400 g) and 11 mice (male, 30-40 g) were deeply anesthetized with isoflurane or ketamine/xylazine. Details of surgery and recovery procedures have been described earlier (Csicsvari et al., 2003). Various electrodes were implanted for unit and LFP recording. All rats and mice were implanted with a microdrive that allowed the positioning of recording electrodes. In 13 rats, linear silicon probes (NeuroNexus Technologies, 16 recording sites at 100 μm vertical spacing) were implanted in somatosensory/parietal cortex and the CA1 pyramidal layer of the dorsal hippocampus (Sirota et al., 2003). In one rat, a single shank linear silicon probe was implanted in the medial prefrontal cortex. In four rats, high density 8-shank ‘octrode’ (15 μm spacing), 64-site probes, (Bartho et al., 2004) were implanted in the medial prefrontal cortex (AP 3.0-4.4, ML 0.5) and posterior hippocampus. In 3 rats, 6-shank, 96-site linear probes were implanted in the parietal cortex in the right hemisphere parallel to the transverse axis of the hippocampus (45° parasagittal) with the outer shanks targeted at approximately (AP -2.8, ML 2.7), and (AP -3.86, ML 1.64) with tips in the CA1 pyramidal layer of the dorsal hippocampus (Montgomery and Buzsáki, 2007). The position of the electrodes was confirmed histologically. In 4 rats and 11 mice 2 to 8 independently movable wire tetrodes were implanted in the parietal cortex and hippocampus (Sirota et al., 2003; Zugaro et al., 2005). In all chronic experiments ground and reference screws were implanted in the bone above the cerebellum.

Chronic Animal Behavior

Four rats with electrodes implanted in prefrontal cortex were trained in a working memory task (spontaneous alternation task or odor-based delayed matching-to-sample task in a figure 8-shape maze). The remaining rats were trained to run on a linear track for water reward (Zugaro et al., 2005). In addition, the animals were recorded during sleep in the home cage. Spectral features of the LFP were used to segment the recording session into periods of REM sleep and awake running (“theta-associated behaviors”; Figure S1). Analysis was performed on 95 REM sessions and 34 waking run sessions. In 27 cases, data from the same set of neurons was recorded during both REM and waking sessions.

Acute Experiments

Experimental details for the acute experiments, along with other data from the same animals, have been published (Isomura et al., 2006).

Data Acquisition and Processing

Extracellular signals were amplified and filtered by multi-channel AC amplifiers (Sensorium EPA5 or RC Electronics; 1000x; 1 Hz to 5 kHz). The intracellular signals were amplified with a DC amplifier (Axoprobe 1A; Axon Instruments). Wide-band extracellular and intracellular signals were digitized at 20 kHz sampling rate with 16-bit resolution and stored for offline analysis using one or two synchronized 64-channel DataMax Systems (RC Electronics, Santa Barbara, CA, USA). Raw data were preprocessed using a custom-developed suite of programs (Csicsvari et al., 1999). The wide-band signal was downsampled to 1.25 kHz and used as the local field potential signal. For spike detection, the wide-band signal was high-pass filtered (>0.8 kHz). Single units were isolated semi-automatically by a custom-developed clustering analysis program KlustaKwik (<http://klustawik.sourceforge.net>) (Harris et al., 2000) and refined manually using custom-made software (<http://klusters.sourceforge.net>; <http://neuroscope.sourceforge.net>; Hazan et al., 2006). For tracking the position of the animals, two small light-emitting diodes, mounted above the headstage, were recorded by a digital video camera and sampled at 30 Hz. Malfunctioning recording sites (e.g., due to high impedance, cross-talk or short circuit) were removed from the analysis (shown in gray in the plots in Figures 3,4,5,6 and 8). Current-source density (CSD) was calculated using a robust second derivative approximation scheme (Freeman and Nicholson, 1975). Spatial smoothing with a triangular kernel was applied to remove spatial noise that stemmed from the variability of electrode impedances.

Data Analysis

LFP, extracellular unit activity and intracellular data were analyzed, unless stated otherwise, by custom-written, MATLAB-based programs. Processing was done either on a stand-alone Linux server or using a Linux cluster (ravana.rutgers.edu; the authors thank Yaroslav Halchenko, Department of Psychology, Rutgers University, for professional cluster administration).

Monosynaptic Connections

For the identification of excitatory and inhibitory connections between neurons, short-latency, short-duration sharp peaks/troughs in the cross-correlograms were used (Bartho et al., 2004; Constantinidis et al., 2001; Csicsvari et al., 1998). Monosynaptic connections between pairs of units were detected using a custom-made interactive software followed by a non-parametric significance test based on jittering of spike trains for computation of the global significance bands (Fujisawa et al., 2008). Significant peaks ($p < 0.01$) within 5 msec of the center bin were considered as putative excitatory monosynaptic connection. Similarly, short-latency troughs were considered to be due to inhibition when at least two neighboring 1 msec bins were significantly depressed. For cell pairs recorded from the same electrode, the 0-1 msec bin was not considered, because our clustering program cannot resolve superimposed spikes.

Cell Type Classification

For each unit, various parameters were calculated, including 1) filtered (0.8 kHz – 5 kHz) spike waveshape parameters: trough to right (late) peak, trough to left (earlier) peak and half amplitude width, asymmetry index (ratio of the difference between right and left baseline-to-peak amplitudes and their sum), 2) firing rate 3) features of the auto-correlogram. Next, we explored the multi-dimensional space formed by these parameters for the subset of units identified as inhibitory or excitatory based on cross-correlogram analysis as described above. The parameters that allowed best separation between the two putative anatomical groups were the trough to right peak latency (related to the repolarization of the intracellular action potential; Henze et al., 2000) and asymmetry index (possibly reflecting differences in the rate of fall of spike repolarization). We used the hyperplane that divided the two physiologically identified classes (interneurons and pyramidal cells) to separate units into putative interneurons and putative pyramidal cells. No attempt was made to distinguish between different types of pyramidal cells or among the large family of interneurons (Markram, 2006; Somogyi et al., 1998). The reliability of our physiological classification method will require anatomical verification of the putative neuron types in future experiments.

Theta Phase Extraction

LFP in CA1 pyramidal layer was filtered with multitaper filter with bandwidth of 1 Hz whose pass-band range was adapted to the instantaneous (within 1 sec window) frequency of theta. Instantaneous theta phase was estimated by Hilbert transformation of the filtered signal. This procedure ensured that prior distribution of phase is uniform (the prior distribution of phases in each session was tested for uniformity prior to unit analysis), since otherwise all circular statistics should be corrected for the bias (Siapas et al., 2005). Although such definition of phase does not take into account waveshape asymmetry, we believe it is a more conservative approach because waveshape asymmetry depends on filter settings, instantaneous theta power and frequency and it varies in time. Nevertheless, we performed all circular statistics tests with non-uniformity bias-correction procedure as described in Siapas et al (2005) and these tests were congruent with our more conservative approach.

Phase Modulation Analysis

First, we used the standard Rayleigh test for uniformity of the phase of unit firing. This test is the most powerful invariant test of uniformity against the von Mises alternative. Rayleigh test is equivalent to a likelihood ratio test, and the statistics of this test $2R^2/n$ (R - resultant length, n - sample size) has an asymptotic chi-square distribution with 2 degrees of freedom (Jammalamadaka and SenGupta, 2001; Mardia and Jupp, 2000). Therefore the appropriate statistics for significance test is $Z=R^2/n$, or variance-stabilized $\log(Z)$. Since statistical distribution is only true asymptotically, the size of the sample can also be a factor (for small n). We performed Monte Carlo simulations to test the performance of Rayleigh test for small samples and found that p-values were in very close agreement for even very small sample sizes. Once the sample is rejected (i.e., nonuniform), one must realize that the sample estimate of resultant length R is strongly biased upwards, and this bias increases as the sample size decreases. Therefore, all measures derived from R , such as the mean resultant length (R/n) and maximum

likelihood (ML), estimate of the concentration coefficient of von Mises distribution (k) and $Z = R^2/n$ have a bias, which depends on the sample size if the sample is drawn from a nonuniform circular distribution. Therefore, the use of these parameters as quantifiers of the modulation strength is not appropriate for small samples. We used Monte Carlo simulations to estimate the sample size at which bias in the estimate of R is sufficiently small. We find that for sample size >1000 the bias in the estimate of R can be neglected. Thus, for comparison across cells and conditions we used concentration coefficient k estimated for subpopulation of cells which emitted more than 1000 spikes (Figures S2,9). We used both conventional maximum likelihood estimate of k and maximal marginal likelihood estimate (Schou, 1978), which has much lower bias for small sample sizes. Both estimates agreed well for sample sizes above 1000.

Another issue in this context is the alternative model of Rayleigh test, the von Mises distribution. This is an important consideration because phase-modulation of unit firing may not follow von Mises distribution, e.g., it could be skewed or multimodal. Thus, the Rayleigh test for uniformity is biased to a degree at which the alternative is not von Mises type, and can be biased depending on cell firing pattern and state. This will also affect the dependence of R and measures derived from it on the sample size. To alleviate some of these issues, we performed additional tests: nonparametric goodness-of-fit Kuiper's and Watson's U^2 tests (Jammalamadaka and SenGupta, 2001; Mardia and Jupp, 2000), which test for uniformity against any alternative. Both tests statistics were correlated with Rayleigh $\log Z$ ($r > 0.9$, $p < 0.00001$), suggesting that model choice was not a determinant factor (Figure S2). Finally, we computed bootstrap Rayleigh tests by subsampling each sample 500 times with a subsample of size 100, which allowed ruling out the effect of sample size on the Rayleigh statistics. This approach, however, is dramatically reducing the power of the test for cells with high sample size. To this end, we have no rigorous resolution for this problem.

Variations in the sample size and contamination of spike train, and therefore a bias on the estimates of R , could arise from imperfect spike sorting. We tested for systematic correlation between the Rayleigh statistic $\log Z$ and cluster quality measure (eDist (Harris et al., 2000)). Cleaner clusters tended to be associated with stronger modulation of putative interneurons ($r = 0.21$, $p < 10^{-5}$), whereas for pyramidal cells there was no such trend ($r = -0.001$, $p = 0.45$). This could be explained by the generally smaller amplitude of interneurons and their stronger contamination by noise (including multiple unit activity of more distant neuronal populations and instrumentation noise). Noise-contaminated clusters effectively decrease theta phase-modulation because non-biological noise is independent of theta phase and firing of other neurons may have different phases than the clustered neuron. In summary, noise contamination may have underestimated the degree and percentage of significantly modulated interneurons, but it did not affect the results for putative pyramidal cells.

Coherence analysis between hippocampal LFP and neocortical spike trains provided a frequency resolved measure of theta modulation of spiking activity in the neocortex (Figure S3) and was, in general, comparable to circular statistics.

The significance of theta modulation can be assessed by using binomial distribution for the number of rejections of uniformity hypothesis at any given alpha level. For example, for pyramidal cells in the parietal cortex the number of rejections of uniformity at alpha=0.05 was 12%, whereas the expected chance level is 5%. The significance of the excess of the number of rejections is determined by the probability to observe 12% (K=63 cells), given the null distribution (binomial with p=0.05 and N=522). This result is very significant (from the binomial distribution we obtain p-value<10⁻¹⁰; using normal approximation of binomial distribution we obtain Z-score of observed number of rejections 7.4). Similarly, for alpha=0.01, the observed rejection percentage is 4%, which yields p-value<10⁻³⁴, z-score =9.1; for alpha=0.001 z-score=17.4. It is clear from Figure 2E that as alpha is decreasing the excess of rejections beyond chance is becoming increasingly significant. For example, there were 9 pyramidal cells (1.7%) with p-values <0.0001; this corresponds to the z-score of ~39!

Mixture Model Fit

For a subset of significantly nonuniformly modulated neurons we tested whether their spike phase distribution is better described by Von Mises distribution, or a more general model, a mixture of Von Mises and circular uniform distributions. The procedure was as follows:

Step 1: Test for uniformity against von Mises alternative (Rayleigh test)

Step 2: If uniform is an adequate model (p > 0.05), analysis was discontinued.

Step 3: Otherwise, test for “von Misesness” against the mixture alternative using likelihood ratio test

Step 4: If von Mises model is adequate, the analysis was terminated and the von Mises model was used. Goodness of fit test was performed based on Watson's U² statistic.

Step 5: Otherwise test the fit of mixture model (using goodness of fit test based on Watson's U² statistic; we did not consider models more complex than the mixture model)

Step 6: If mixture model was adequate, then the mixture model was used.

The above-mentioned sequence of tests was performed using a code in R language provided by John Bentley (Bentley et al., 2007). For ~11% of neurons the likelihood ratio test argued in favor of the mixture model. For the remaining neurons a simpler model (von Mises) provided an adequate fit. Because the firing of every neuron is driven presumably by a combination of phase-related and phase-independent inputs, a mixture model may be more accurate from the physiological point of view for the description of phase-modulation.

Spectral Analysis

Unit and LFP power spectrum and unit-unit, unit-LFP, and LFP-LFP coherence estimates were performed using multitaper direct spectral estimates. For theta frequency range, we typically used window sizes of 1-2 seconds and 3-5 tapers, and for gamma range – 50-200 msec and 5-9 tapers. Estimates that involved units were made only on windows that contain at least as many spikes as tapers used (Jarvis and Mitra, 2001). For coherence estimates we verified homogeneity assumption in a selected set of data by comparing the error bars computed by jackknife and theoretical estimate.

Spatial localization of gamma coherence requires, strictly speaking, multiple comparison tests for testing significance. Due to clear topographic localization of LFP with significant peaks at the same gamma frequency, we are confident that most permutation tests would show a significant effect.

In addition to coherence estimates, we also performed phase-locking index estimation (equivalent to Rayleigh test for each frequency bin) and power correlation. These two measures are combined in the coherence measure due to nonstationarity of power across windows. Invariably, increase in coherence at a certain frequency and location was associated with increased phase-locking at the same frequency and location.

Unit-triggered average spectrum was computed in 200-msec windows at different time lags from the time of spike for every recording site. The “baseline” spectrum calculated for the entire session was subtracted from the unit-triggered spectrum for spatial localization analysis to estimate the deviation of the spectrum during unit firing from the overall mean. In some cases, increase in absolute gamma power was more prominent in the hippocampus than at neocortical sites. This could reflect a non-Poisson and nonwhite statistics of unit firing and gamma power. Unit-triggered average spectrum is equivalent to a correlation coefficient between the binary process of unit firing and gamma power at every frequency bin. As such, it is not known whether both unit firing and gamma power are co-modulated by hippocampal theta. In the frequency domain, the cross-correlogram is equivalent to cross-spectrum, which contains both amplitude correlation and phase-locking between the two signals. In our analysis the primary goal is to reveal neocortical gamma sources associated with unit firing. Therefore, power spectra of unit firing and gamma power may confound the strength of the phase relationship between unit activity and gamma oscillations—the goal of the analysis. Moreover, for different recording sites the magnitude of gamma power modulation by theta phase may vary. Finally, volume conduction of LFP is a further potential confound. Due to these considerations, unit-triggered spectral analysis is adequate only for neurons that are not very strongly modulated by hippocampal theta and can be reliably associated with a single gamma source.

Theta Modulation of Gamma Power

The predictable effects of volume-conduction can be exploited in some special cases to support our general conclusion regarding the hippocampal theta modulation of neocortical gamma oscillations. High frequency gamma (>100 Hz) was well defined in the neocortex but weaker in the hippocampus. Importantly, there was a clear gap in the spatial profile of power in the high gamma band between neocortical locations and the hippocampus (not shown), an convincing argument against volume conduction of hippocampal gamma to the neocortex, at least for higher frequencies. We estimated gamma power at all cortical locations in short (50-100 msec), temporally overlapping sliding windows and determined the magnitude of theta modulation of the resulting signal at every gamma frequency bin by calculating the coherence between LFP in the CA1 pyramidal layer and gamma power time series in the respective frequency bin.

Local Maxima of Gamma Power

To detect isolated gamma bursts in the neocortex, we limited our analysis to gamma bursts, which were localized in space, frequency and time and were sufficiently well isolated in these dimensions from other gamma bursts. These events were identified as local maxima in the 4-dimensional (time x frequency x shank number x site number) matrix of spectral power (Figure 4D). This constraint allowed the segregation of gamma bursts in terms of their spatial and frequency localization and the examination of their theta modulation. Although this approach limits the analysis to gamma bursts with no contiguity in any dimension to other gamma bursts, it avoids the problem of linear mixing of different gamma sources. Using this approach, we obtained sufficiently large numbers of gamma bursts in many of our datasets. The local maxima of these gamma bursts demonstrated a clear nonrandom clustering in space (Figure 4F) and frequency. Because frequency had a clear bimodal distribution (Figure 4E), we divided gamma bursts into fast and slow (above and below 100 Hz) events. This classification yielded 5-15 clusters in a dataset, each with localized spatial and frequency properties. The time of occurrence of gamma bursts from individual clusters was then used in the theta phase modulation analysis.

Gamma Frequency-Location (gFL) Factor Analysis

gFL factor analysis consists of the following steps:

1. Whiten the LFP from all recording sites. Perform autoregressive model of the second order with coefficients vector A that fit to the data. This low order model essentially fits the “pink” shape of the spectrum ($\sim 1/f$). Then a filter $[1; -A]$ is used to filter the LFP signal to remove the pink component. Whitening essentially equalizes the variance across frequency bins and decreases frequency leakage during spectral estimates. The same whitening model is used for all sites.
2. Compute spectrum of whitened LFP for each site in the range of 30-150 Hz for overlapping 100 msec windows stepping by 13 msec (steps of 20, 50 and non-overlapping windows were also tried and did not yield different results, but reduced the temporal resolution of the method needed for analysis) that cover all robust theta epochs (during REM or RUN session). As a result we obtain nCh matrices of size $nVariables = nF * nT$, where nCh – number of sites, nF – number of frequency bins, nT – number of time bins.
3. Log-transform the matrices to bring marginal distributions for each variable (frequency bin on one channel) to a more symmetric form (closer to normal). Concatenate spectral matrices along frequency dimension to form a matrix M of size $(nF*nCh) \times nT$. Here $nF*nCh$ – number of variables for future multivariate analysis and nT – number of samples.
4. Perform PCA on matrix M , leave 99.9% of the variance in the model. This gives a matrix of principal component eigenvectors W . Since gFL analysis concerns only the small subspace (spanned by ~ 30) eigenvectors, corresponding do largest eigenvalues, the amount of data ($nT/nVariables$ ratio was between 10 and 100) were large compared with the size of this subspace, and the subspace was well populated by data.
5. Perform orthogonal rotation of the matrix W using the Varimax method (Kayser and Tenke, 2003; Reymont and Joreskog, 1993), employing simplicity criteria to

- obtain a matrix of factor loadings. The goal of simplicity criteria is to obtain factors with only a few high loadings and near-zero loadings for the majority of variables. Such rotation turns factors from simply spanning the directions of largest variance, which are not physically meaningful, into factors that capture a parsimonious structure in the covariance matrix and is more likely to be physiologically meaningful. In short, the essence of the method is this: rotated factors will correspond to the directions in the spectral space, which span limited frequency bins at a few sites with strong covariance. Another benefit of the method is that factor loadings are always non-negative, thus it eliminates the ambiguity of the sign of the factor loadings present in PCA.
6. Compute variance explained by rotated factors, factor scores – projection of the data on the rotated factors.
 7. For further analysis, we computed only the first 30 factors because the first 5-20 factors explained most of the variance. This procedure is likely to result in an underestimation of the true number of factors. Factors that had high loadings on only 1 or 2 frequency bins or 1 or 2 dispersed sites were considered artifacts and removed from the analysis. Factors with maximal loadings on the boundary frequency bins stem from spectral leakage from lower or high frequency ranges and were also removed.
 8. We further determine the location of the maximum loading of each factor in frequency and location. The latter is estimated as the center of mass in anatomical space covered by the recording sites. Most factors produced highest loadings concentrated around one frequency bin and one anatomical location. Frequency and location of the gFL were typically independent of each other. Therefore, for each factor we compressed the $nF \times nCh$ vector of factor loadings (Figure 4D) into two vectors (profiles) – Frequency profile (factor loading across all frequency bins at maximal loading location) and Location profile (factor loading across all sites at the maximal loading frequency bin). Factors were classified as neocortical or hippocampal depending on the anatomical location of the maximal loading.
 9. Factor scores were computed by projecting the original spectral matrix on the factor loading vector. To reduce the contribution of the gamma power away from the gFL center we set the factor loading values to zero for all elements with loading below 15 percentile. In mathematical notation, if X is original data matrix, A is a matrix of factor loadings and S is a matrix of scores, we are seeking decomposition $X=A*S+e$, where e is an error term. To obtain the score matrix given a matrix A (“project” the data X on A) we computed the pseudo-inverse of A and multiplied it with the data matrix X : $S=A^{-1}*(X-e)$. Time series of the factor score represents the change of weight of the factor across time. Thus, this continuous variable can be interpreted as the “strength” of gamma oscillation characterized by both Frequency profile and Location profile (gFL). Coherence between gFL score and LFP was performed using multitaper estimates as described above. LFP signal was resampled at time stamps centered on the spectral windows used to compute the spectrograms (see step 2).
 10. Peaks of gFL scores are detected as local maxima separated by at least 50 msec and above 75 percentile of the overall score distribution. Peak times represent the occurrence of the gamma “burst” characterized by Frequency and Location

profiles. Circular statistic analysis was performed on theta phase at the time of gamma bursts for each gFL. We found no correlation between the Rayleigh statistic $\log Z$ and variance explained by the gFL factor ($r \sim -0.06$), indicating that gamma bursts were theta modulated independent of how prominent they were.

Partial Coherence Analysis

Since projection of the large gamma power from sites with small loadings (hippocampal sites) can still bias the gFL score due to possible volume conduction from hippocampal sites, we computed partial coherence between the neocortical gFL score and LFP by partializing it by the gamma power in CA1 pyramidal layer, filtered according to the frequency profile of the respective gFL. Partial coherence was considered non-significant if its values at theta frequency band fell below the significance level determined from full coherence. Clearly, the larger the power of hippocampal gamma, the stronger the effect of volume conduction to the neocortex, but the converse is also true – the larger the power of neocortical gamma (which is the case for low frequencies), the more it contributes to gamma power measured in CA1 pyramidal layer. This may result in significant decrease of partial coherence value – false negative result.

Theta Modulation of LFP-LFP Gamma Coherence

A limitation of gFL factor analysis is that it is based the spectral power, which limits one's ability to perform linear unmixing of the individual gamma oscillators. Addition of phase information to the analysis would strongly improve the method, but requires further improvement of this method, a goal which lies beyond the scope of this paper. Importantly, the gFL analysis should be considered as an effective exploratory tool to identify the location and frequency of individual gamma oscillators but it must be validated by spectral analysis which includes phase information of the signal.

For each gFL we validated the analysis in the following way. We computed coherence between the LFP in the center of the gFL-identified spatial gamma profile (center of mass of spatial factor loading) and the LFP at all other recording sites. We used spectral windows of 50 msec and 9 tapers. The average coherence over the entire session typically had a significant peak at the frequency close to preferred frequency of the gFL and had spatial profile at this frequency that matched that of the gFL in question (Figure 6J), providing a phase-synchronization measure of the local neocortical gamma. Analysis of the spatial coherence maps allowed us to determine the presence or absence of local oscillations. If no local oscillations are found in the center of gFL, presumably due to volume conduction from elsewhere (e.g., from hippocampus), the coherence between the center and the location of source of gamma currents (local-distant) is expected to be higher than between the center and nearby locations (local-local). Thus, in case of volume conduction the spatial profile of coherence at gamma frequency would have a maximum away from gFL center. Since there are always some locally generated currents, albeit with flat (white or pink) spectrum, the local-local coherence across all the frequencies may be higher than that of local vs. distant. However, this would be true for any frequency bin. In short, presence of high coherence in a narrow frequency band spatially confined to the center of gFL can be considered as evidence for locally generated gamma.

To test whether hippocampal theta modulates neocortical gamma, we can use the spatial profile of gamma band coherence as a measure of local gamma synchronization. The logic behind this approach is as follows. Let us assume that there are two gamma oscillators (local-neocortical and distant-hippocampal), the power of the local one is not modulated by theta, whereas the power of the distant one is modulated. Then, on average, local-local coherence is maximum around the center of neocortical gamma in a frequency band of neocortical gamma. Now we can compute the gamma band coherence in short moving windows and quantify the coherence of these time series to the theta LFP in hippocampus ('coherence of gamma coherence' measure). The temporal fluctuation of the local-local coherence is coherent with theta oscillations since both local sites at the gamma source detect the volume-conducted signal from the distant theta modulated gamma source, but the coherence of the fluctuation of local-distant gamma band coherence with theta must be stronger, because it is less contaminated by non-theta related local gamma. Thus, the spatial profile of the coherence of gamma band coherence fluctuation to theta (i.e., theta modulation of gamma synchrony) should have a maximum at the source location of theta modulated gamma, and not locally. If, on the other hand, the local neocortical gamma is modulated by theta, we should expect to see maximum coherence of gamma coherence fluctuations to theta at the center of neocortical gamma oscillator. To quantify this relationship, we computed the integrated LFP-LFP coherence within the preferred gFL frequency band in short running windows (50-100 msec) for the entire session, and estimated the coherence between this time series and hippocampal LFP for each pair of all recording sites. We determined the similarity between the spatial profile of the coherence of gamma coherence to the spatial profile of average gamma coherence and the gFL spatial profile in all sessions recorded with 96-site silicon probes, which provide 2^d spatial coverage of both neocortex and underlying hippocampus. In only a few cases we found that maximal coherence of gamma coherence was localized away from the center of respective gFL, indicating that that theta modulation of gamma oscillation occurred elsewhere in the neocortex, independent of the sample gFL. In most cases, however, gFLs and the coherence profiles strongly overlapped, indicating that the power of local neocortical gamma is theta modulated. Thus the effect of volume conduction from any other gamma sources can thus be ruled out in this analysis (e.g., Figure 6K).

Potential Caveats of the Gamma Analysis

Gammas oscillations in the neocortex are typically transient and small amplitude. Detection and isolation of such small amplitude signals often require high spatial resolution methods and complex mathematical-statistical procedures. Because of such complexities, no straightforward tools can be offered. Below, we address some of the caveats and solutions of the methods used in our analyses.

What Is the Effect of Whitening of the LFP Prior to Spectral Analysis?

There are two main reasons for whitening the signal in our analysis. First, whitening reduces the dynamic range of the signal and thus reduces the leakage of low frequencies into the higher frequency bins during spectrum estimation. This reduces the bias in the spectrum estimation (Pesaran and Mitra, 1998). Second, we wanted the variance at different frequency bins to be the same and their contribution to the covariance matrix

comparable. Whitening adjusts the $\sim 1/f$ falloff of the spectral power with frequency, which is mostly the consequence of the fact that slower frequencies can synchronize over large spatial domains and result in larger amplitude signals. It is not the exact power of the gamma oscillations in different frequency ranges, but their temporal dynamics, that we aimed to explore, and thus we did want to make their contributions to the covariance matrix independent of their absolute amplitudes. There is no physiological reason to believe that signals of lower power are less important than signals of high power, given that they may have different physiological mechanisms. Covariation between power values at different recording sites and frequency bins reflects the presence of oscillatory source located around these sites with peak power at the corresponding frequency range. In statistical terms, whitening is aimed to standardize the data at different frequency bins before the factor analysis, a standard procedure in multivariate analysis (e.g. Krzanowski: Principles of Multivariate Analysis).

How Do Harmonics of Theta Confound the Analysis?

First, the whitening procedure equally emphasizes theta harmonics and genuine gamma oscillations, hence whitening makes no difference for the gamma range analysis. Second, the maximal power of higher harmonics of theta in the gamma range do not reach, on average, more than $\sim 20\%$ (for 2nd) and $\sim 7\%$ (for 3rd, 32-40 Hz) of the average theta power at the fundamental frequency. Contributions of higher harmonics are much smaller. Therefore, the putative contribution of theta harmonics is limited to the low range of gamma frequency band ($<40\text{Hz}$). In contrast, the strongest theta phase modulation, according to our various analyses (gamma power, gFL and LFP-LFP coherence modulation), was observed at higher frequencies ($>100\text{ Hz}$), which could not stem from higher harmonics of theta oscillations. Furthermore, if theta harmonics artificially generated gFL factors they would have a center of mass in the hippocampus and not in the neocortex. Third, since the power of theta harmonics is independent of the power of true gamma oscillations, individual gFLs that could stem from theta harmonics could be easily identified. During the screening of gFL factors, we removed all factors with maximal loading in the lower frequency bin (30 Hz). Likewise, we did not detect local maxima of spectral power with isolated power below 30 Hz.

Is the Covariance Matrix Well-Conditioned and Does It Affect the gFL Analysis? How Robust Is the Method?

As discussed in the gFL method section, the number of data points was much larger than the number of variables. Due to volume conduction, the covariance matrix cannot be under-populated. Nevertheless, because of putative volume conduction and comodulation of gamma oscillators the covariance matrix suffers from multicollinearity and has high condition number. However, ill-conditioning of the matrix will only surface during the inversion. Neither PCA dimensionality reduction nor the Varimax rotation will be affected by the high condition number of the matrix, because they do not include the covariance matrix inversion. The ill-conditioning of covariance can be reflected in the estimation of the sources for the smallest eigenvectors. In fact, one of the methods to regularize ill-conditioned matrices is based on truncation of smallest eigenvalues in SVD (e.g. P. C. Hansen: Rank-Deficient and Discrete Ill-Posed Problems: Numerical Aspects of Linear Inversion). Furthermore, we constrained the Varimax rotation to the subspace

spanned by the first r principal components, where r is the number of eigenvalues larger than 10^{-4} . Typically, r was slightly smaller than number of variables. Since our analysis uses only highest (typically less than 20) eigenvectors, they will not be affected by ill-conditioned covariance matrix.

In addition, we ran several tests on our data. First, we computed Kaiser-Meyer-Olkin Measure of Sampling Adequacy (Kaiser 1970, 1981), which indicates whether the data factors are well based on correlations and partial correlations between the variables. For all data sets, this statistic was above 0.85 (mean = 0.95, std = 0.02). Random data would correspond to 0.5 and values >0.8 indicate high suitability for factor analysis. It is clear from this analysis that ill-conditioning of the covariance matrix is in fact correlated with its suitability for factor analysis. Second, we split the data in two halves and compared the covariance matrices. To do so we computed single value decomposition and compared the eigenspectra of the covariance matrices for two halves of the data set. The relative difference between eigenvalues was $2\% \pm 1.8\%$, which indicates that we have sufficient amount of data to get consistent estimates of the covariance matrix. Analysis of eigenspectra differences showed consistent increase in the relative eigenvalue difference towards the end of the eigenspectra (i.e. for small eigenvalues), which further supports our contention that the variability/errors in the covariance matrix estimation corresponds to the small eigenvalues, and thus will not affect the PCA or Varimax rotation.

We could not perform a full 10-fold cross-validation due to constraints of sample size, but we did perform the entire gFL analysis in first and second halves of all datasets. We found a close correspondence between the factor loading vectors obtained from full dataset and either half (Figure S9). The consistency between the two halves of data support our conclusions that (a) we had enough data for the proper estimation of the covariance matrix, (b) changes in covariance matrix (first and second half) did not affect the outcome of the analysis, and (c) spatial and frequency profiles were not random or trivial. Equally importantly, the degree of theta modulation of the gFL scores in the first and second halves of data was highly correlated for most of the gFLs, and even the preferred theta phase matched very closely (Figure S9). This means that each gFL score represents the time course of an independent process, which can be theta modulated to a certain degree and at a given preferred phase. This is not expected if any step of the analysis included random (noise, artifact) driven signal. Random noise would not give rise to (a) phase relationship to theta and (b) consistency between the two halves of the datasets. This analysis further argues against the pivotal role of volume-conduction, since volume conduction of hippocampal gamma to different cortical locations would result in *similar* theta modulation strength and phase. We believe this is a strong argument against the alternative that randomness and arbitrariness gave rise to the observed effect in our analyses, and suggests that gFL analysis does perform satisfactory demixing of individual gamma time courses.

Does the Linear Nature of gFL Analysis Introduce Rather Than Alleviate the Problem of Volume Conduction?

Volume conduction results in a linear mixing of different gamma sources. There is no ideal method to perfectly solve this problem. All existing methods are based on linear

transformations. For example, current source density (CSD) method, widely used in neuroscience community, is a linear transformation of voltage values. CSD improves the localization of the current sinks and sources and follows from the Maxwell equations.

First, our analysis was not affected by the imperfections of factor analysis (such as nonzero factor loading in hippocampus for the neocortical gFLs). For each gFL the factors score was calculated by projecting the data on the subspace formed by the sites from the upper 85% of the factor loading values and proximal to the center of gFL. Second, as the goal of linear factorization is to unmix linearly mixed sources. Even though all elements of loading matrix A are nonnegative, some elements of pseudo-inverse A^{-1} are negative, and it is precisely the elements corresponding to gamma frequency bins derived from sites away from the gFL center or preferred frequency (e.g. hippocampal sites) that will be negative. Because of this negative contribution in the linear combination, it alleviates the problem of volume conduction, rather than emphasizes it. Third, the contribution of theta modulated hippocampal gamma to neocortical gamma was also ruled out by the partial coherence analysis. If linear contribution of gamma power at any frequency explained theta modulation of the gFL score, partializing the coherence by the power of hippocampal gamma should abolish the coherence. This was not the case. Fourth, the goal of gFL analysis is exploratory: due to volume-conduction (leading to linear mixing) and variable power of different gamma oscillators it is not possible to determine the location and frequency of gamma oscillators *a priori*. However, factor analysis allows one to uncover the spatial and frequency structure of the diverse arrays of gamma oscillators. This information can be further used to perform more direct analyses (e.g. LFP-LFP coherence) within the uncovered spatial and frequency loci.

Does Current-Source Density Analysis or Local Referencing Eliminate Volume Conduction?

The voltage produced by volume conducting currents decays inversely with distance from the point source. For a spatially distributed source the picture is more complex. Here we are dealing with multiple spatially segregated sources of various size and amplitude. Differential recordings simply measure the voltage difference and could yield significant values even in the complete absence of a local signal. The same problem applies to the combined reference electrode (eg. Nunez and Srinivasan, 2005). Using CSD analyses indeed appears ideal but this approach works well only with single dipoles or with dipoles with fixed phase delays. Attempts to localize neocortical gamma oscillations with CSD analysis routinely has not been successful despite several attempts in various cortical regions and species, at least not with 100 μm electrode spacings. Furthermore, our electrodes were not perpendicular to the layers in PFC and in several experiments only tetrodes were used. In addition, we suggest that irregular cytoarchitecture, multiple layers and the lower cell packing density of the neocortex make spatio-temporal summation of membrane currents of coherently active neurons in the extracellular space less effective than in the hippocampus. Thus one may not expect to observe spatially confined current sources/sinks associated with rhythmic intracortical network activity. In contrast, sleep spindles and evoked responses have sizable current

sinks associated with synchronous activation of the thalamic projections to a confined layer IV neurons.

Is the Space-Frequency Structure of gFLs Simply a Consequence of Particular Linear Decomposition?

The conclusion that gamma oscillations are localized in space and frequency was first identified by the unit-unit and unit-LFP spectral analyses. It was confirmed by analysis of the gamma bursts isolated in space, frequency and time. These observations led us to the gFL analysis. For physically meaningful linear decomposition of the data some constraints needed to be imposed. Such factorization is the goal of the linear methods like ICA, nonnegative matrix factorization, factor analysis, etc. The constraint could be, for example, independence of the scores, which we cannot not assume since individual gamma oscillators are likely comodulated. Varimax rotation imposes a constraint of simplicity of the factors (Thorstone 1935, Kaiser 1974), which is related to sparseness, as discussed recently in the literature of blind source separation. This constraint is compatible with the spatial and frequency tuning of gamma oscillations observed by independent methods, as spelled out above. Moreover, nowhere in the method is the contiguity of large loading values in space and frequency imposed, yet such structure is discovered by the method – providing evidence that there is sufficient information in the covariance matrix. Critically, the spatial and frequency tuning of gFL factors closely matched our results of unit-LFP spectral analysis. The exact choice of rotation, even though it is data driven, is not unique, and particular choices we make could affect the outcome. One factor that does affect the outcome is the orthogonality of the eigenvectors imposed by the Varimax rotation. Therefore, on a subset of the data we performed the Promax rotation which relaxes the orthogonality. The majority of salient factors remained, though their numbers decreased. Thus, the observed segregation of gamma oscillators, by frequency in particular, could suffer from excessive splitting. Nevertheless, the orthogonality constraint in our analysis did not lead to false positives in subsequent analyses.

Membrane Potential Analysis

In the analysis of intracellular data, spikes were first removed. To achieve this, an average of the intracellular action potential was computed for each cell and the membrane potential was interpolated around all action potential peaks for the duration of the spike. Integrated gamma power was computed in the 25-55 Hz band as a smoothed rectified filtered V_m. Coherence between hippocampal LFP and the membrane potential or the integrated gamma power in the membrane potential was computed using 3.5 sec windows and 5 tapers. Significance of coherence was tested using jackknife resampling method (Thomson and Chave, 1991). This procedure is necessary in light of strong nonstationarity of power in the theta-band in the membrane potential signal. Coherence was considered significant at $p < 0.01$. The phase shift between the intracellular signal and LFP in CA1 pyramidal layer was taken at the frequency of maximal coherence. Since in several cases LFP was recorded in the dentate gyrus (e.g. Figure 6C,D), we adjusted the phase shift values for these cells in the group display (Figure 6E) by the phase shift between the LFP in CA1 pyramidal layer and dentate gyrus ($\sim 175^\circ$; Isomura et al., 2006).

Where does the large variability of the phase shifts between the LFP and Vm come from? There are several possible explanations for such variability in phase shift compared to the relatively well concentrated phase preference of suprathreshold firing of neocortical neurons in behaving animals (Figure 2 G,H). First, difference in the state of the animal in different experiments and depth of anesthesia could cause differential attenuation of synaptic transmission in hippocampo-cortical circuits resulting in differential phase shift. Second, due to spontaneous changes of the membrane potential over the course of a long recording session the degree as well as phase of locking of the membrane potential of neocortical neurons to hippocampal LFP can vary within and between animals. Third, due to the limited sample size of the intracellular experiments, a high degree of variability of preferred phases between Vm and LFP is expected, similar to the highly variable preferred phases of significantly theta modulated prefrontal and parietal neurons in REM sleep and waking (Figure 2).

Supplemental Figures

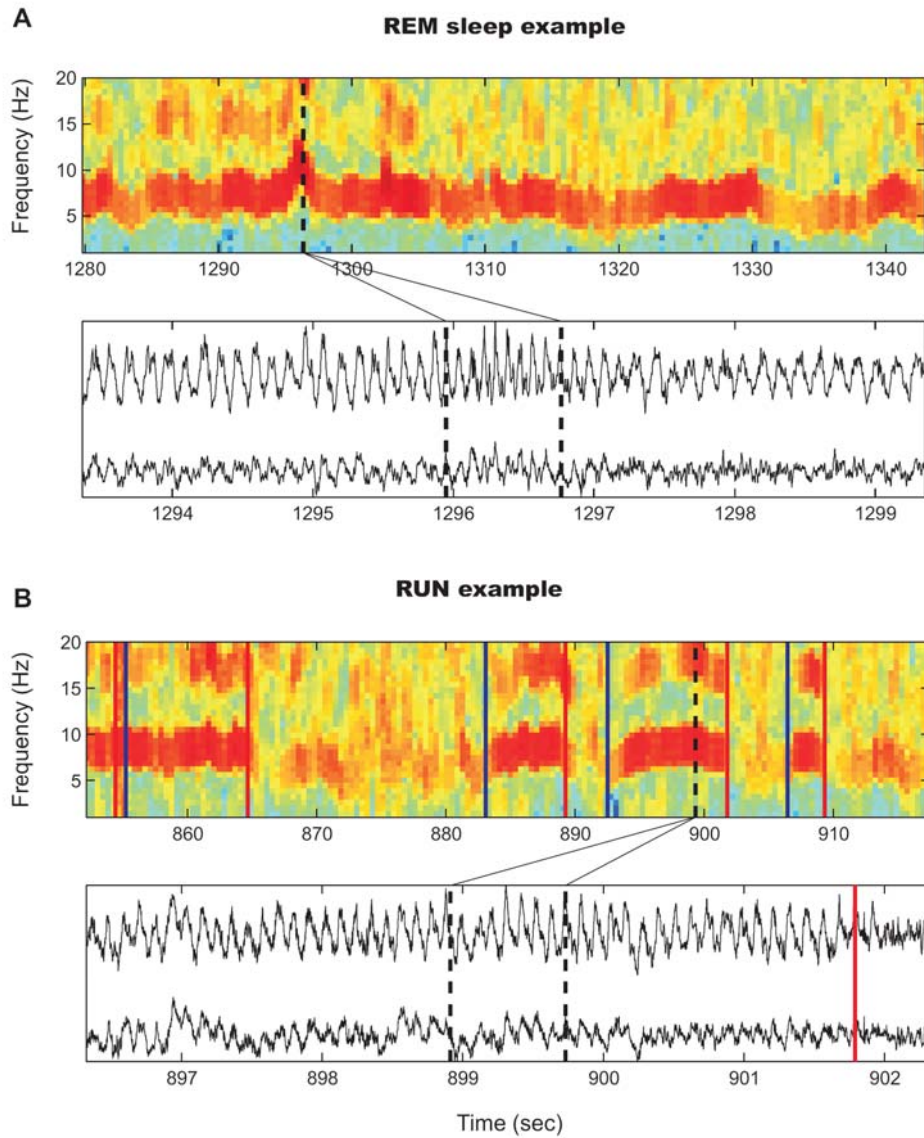


Figure S1. Detection of theta oscillations. Sample spectrograms (top) of LFP recorded in the CA1 pyramidal layer during REM sleep (**A**) and running on an elevated maze (**B**). Traces (bottom plots) display short epochs (dotted lines in spectrograms) of LFP from the CA1 pyramidal layer (top trace) and deep layers of the parietal cortex (bottom trace). Beginning and end of theta episode associated with exploration of the maze is marked by blue and red line, respectively.

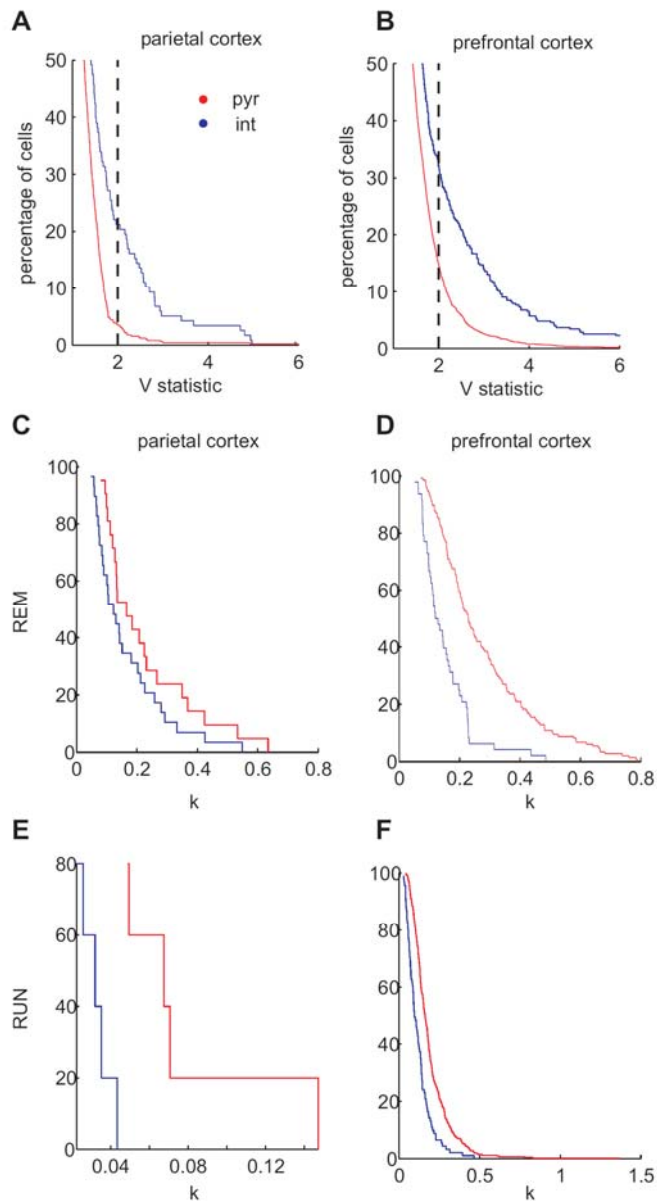


Figure S2. Hippocampal theta modulation of neocortical neurons (additional group statistics). (A,B) Cumulative density plots for Kuiper test V statistics in parietal (A) and prefrontal (PFC, B) cortex. Note that there is higher percentage of significantly modulated interneurons than pyramidal cells. The results from nonparametric test against any alternative therefore confirm results of Rayleigh statistics. (C-F), Cumulative density plots for ML estimates of concentration parameter k for cells with sample size > 1000 for pyramidal cells (red) and interneurons (blue) in parietal (C,E) and prefrontal (D,F) cortices during REM sleep (C,D) and awake running (E,F). Note that pyramidal cells invariably have stronger modulation than interneurons. This is in apparent contrast to the finding that a larger percentage of neocortical interneurons is significantly modulated. These observations may be explained by the different features of the two cell types. Interneurons have lower spiking threshold and are more electrotonically compact, thus their output can be shaped by variety of inputs. Pyramidal cells

are constantly inhibited and only the strongly activated ones reach the spiking threshold. Therefore, if both cell types receive comparable periodic subthreshold inputs at theta frequency (signal), their output may reflect different magnitude of non-theta related inputs (noise). As a result, the signal-to-noise ratio of interneurons may be lower than that of pyramidal cells (lower k), yet the large number of spikes emitted by interneurons in a given recording session provides a higher statistical power when tested for theta modulation.

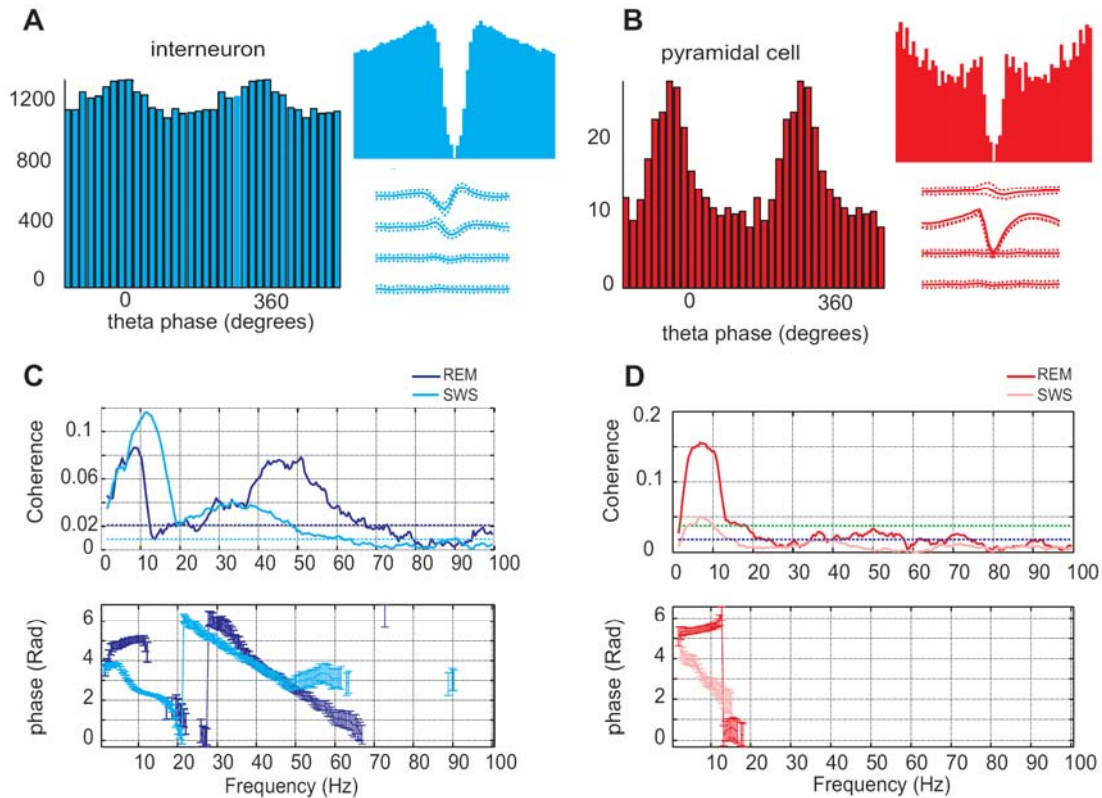


Figure S3. Spectral analysis of theta modulation of neocortical neurons. (A-D), Examples of theta modulation of interneuron (A,C, blue) and pyramidal cell (B,D, red). (A,B), theta phase histograms (left) and autocorrelograms and spike waveshape (right). (C,D), Coherence (top) and phase spectra (bottom) between spike train of respective units and LFP in the neocortex during REM sleep (dark color) and slow waves sleep, SWS (light color). Note peaks in coherence at theta (likely hippocampal theta volume-conducted to neocortex) and gamma frequency during REM sleep and spindle and lower gamma frequencies during SWS. Note linear phase shift with frequency for gamma range (in C, bottom). Such frequency-related phase shift is indicative of a fixed temporal relationship between the mechanisms responsible for gamma LFP and unit firing.

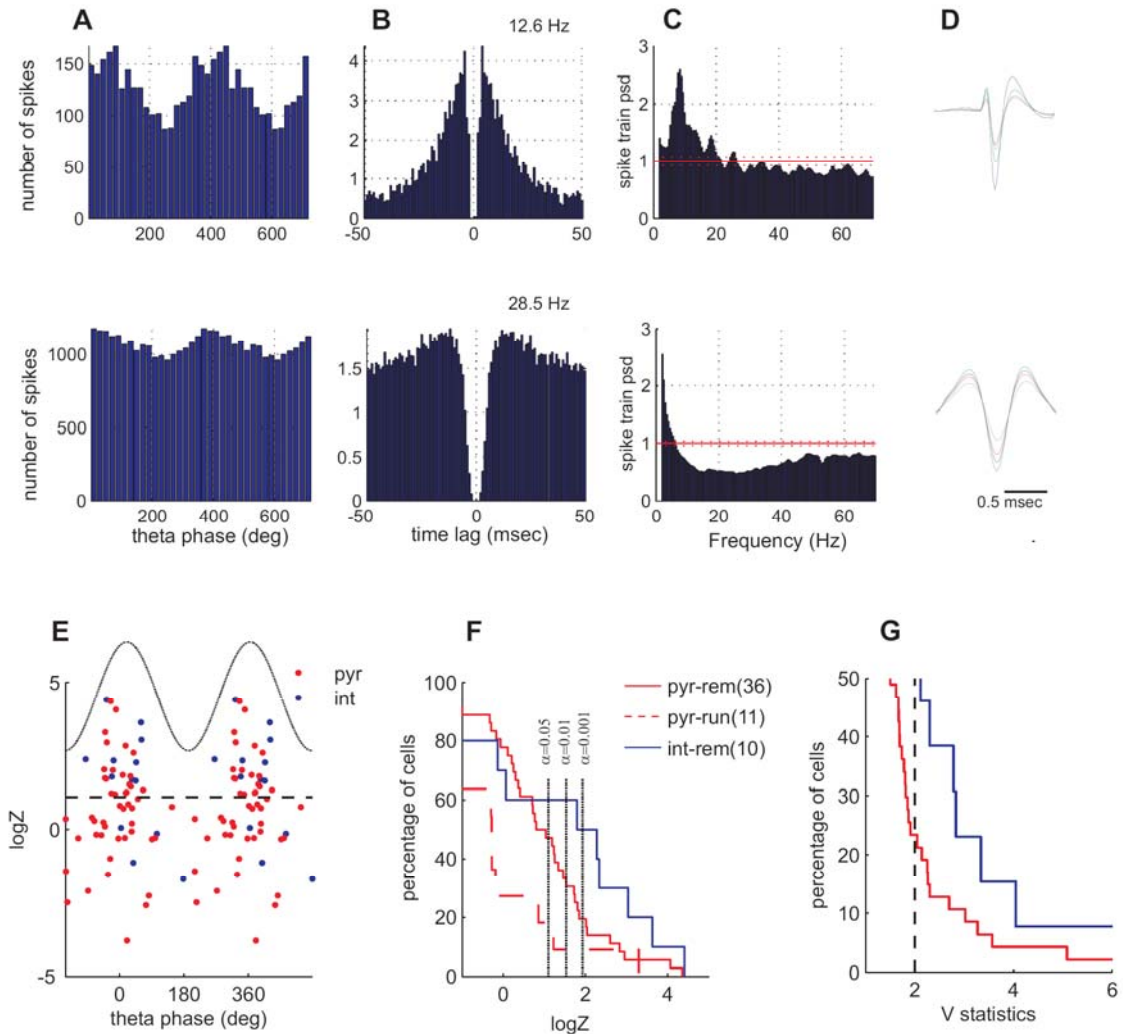


Figure S4. Hippocampal theta oscillation modulates neocortical unit firing in mice. (A-D). Two putative interneurons significantly modulated by hippocampal theta. (A) Theta phase histograms of neural firing. (B) Auto-correlograms of respective neurons. (C) Power spectrum of spike trains of respective neurons. Note a distinct spectral peak at theta frequency for the top neuron. Red solid and dotted lines, mean and SD of the power expected for the Poisson process with the same mean rate. (D) Average filtered (800 Hz-5 kHz) spike waveshapes of the respective neurons. (E) Group data of estimated preferred phase versus Rayleigh statistics ($\log Z$) for all neurons ($n=86$) in 11 mice. 0, 360° , peak of theta in CA1 pyramidal layer. Dotted line indicates the significance threshold for $p < 0.01$. (F) Cumulative density function of $\log Z$ statistic for putative pyramidal cells and interneurons in different states. (G) Cumulative density function of Kuiper V statistic (see Methods) for the same neurons.

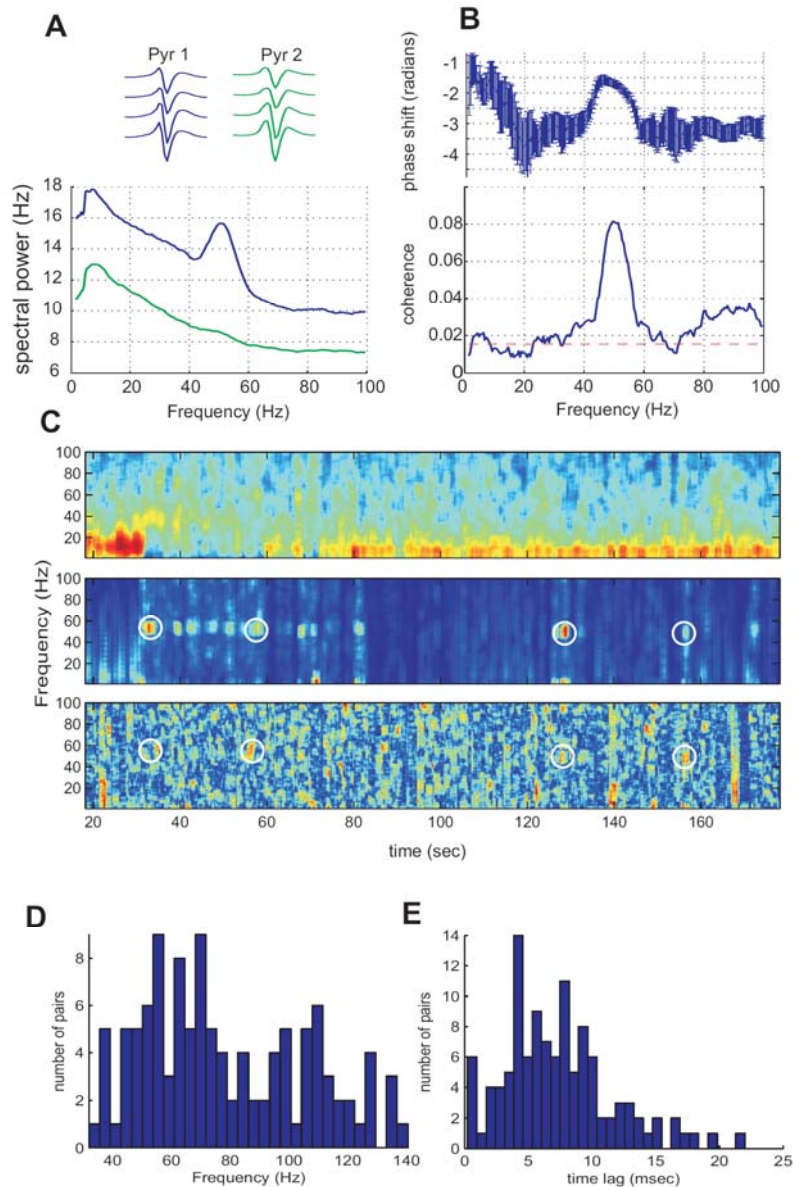


Figure S5. Dynamic gamma synchronization of neocortical neurons. (A-C), Example of a pair of putative pyramidal cells synchronized at ~50 Hz gamma frequency. (A) Power spectra of spike trains of the two pyramidal neurons. Inset, average filtered spike wave shapes. (B) Coherence (bottom) and phase shift (top) between spike trains of the two neurons. (C) Sample time stretch of sleep recording illustrating simultaneous time course of the LFP spectrum (top), spectrum of spike train Pyr 1 (middle) and coherence between the two neurons (bottom). Note transient nature of gamma synchronization. The figure illustrates that simple “overall” average spectral measures may not be adequate to capture gamma frequency coupling between cell pairs or within ensembles of cells. (D-E). Group summary of n=113 pairs of neurons, which were significantly coherent in the gamma frequency band. (D) Distribution of frequency of gamma synchronization. (E) Distribution of time lags between spike trains of gamma-coherent pairs of neurons. Time lags are inferred from the phase shift at the peak gamma frequency.

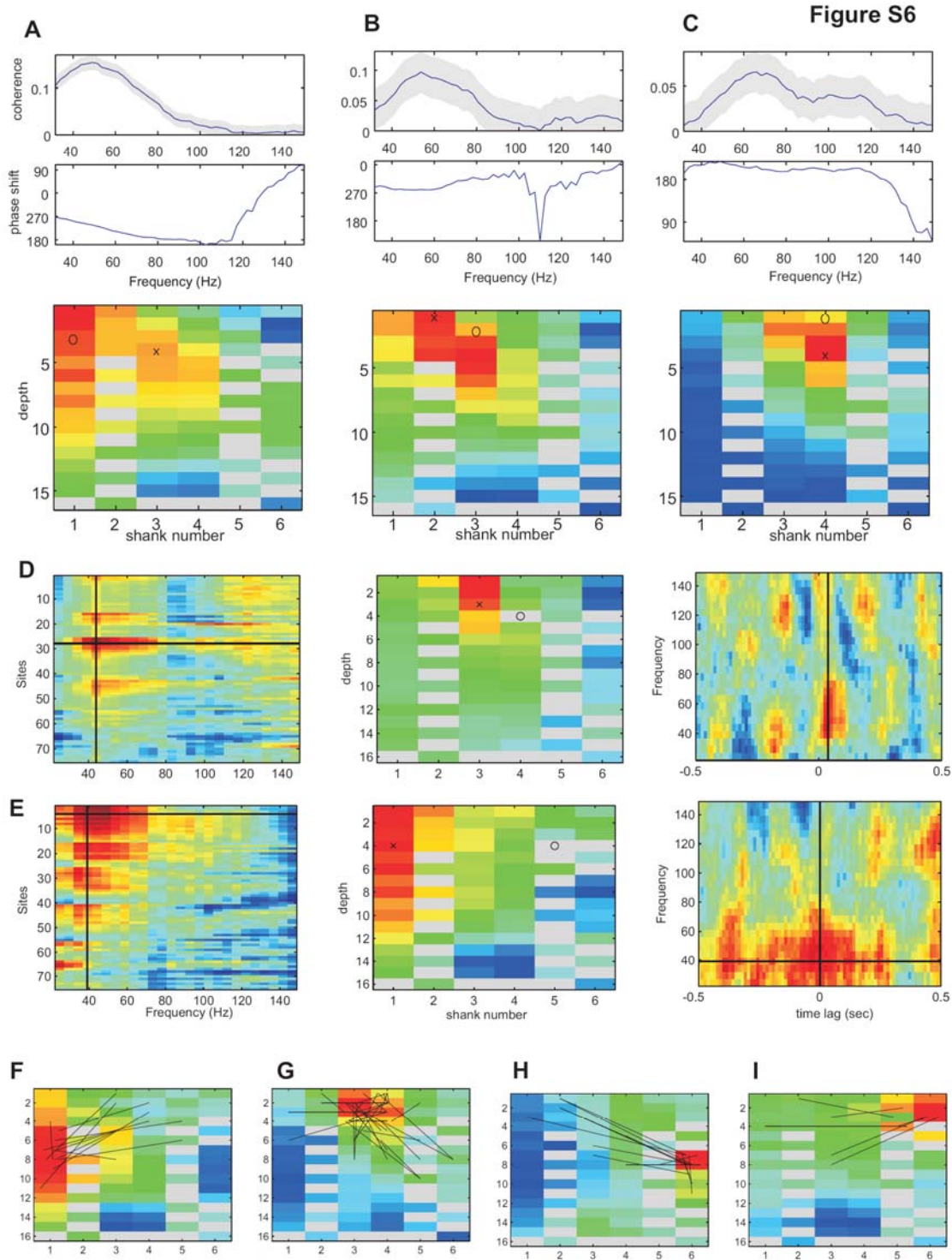


Figure S6. Unit-triggered spectral analysis of gamma oscillations. (A-C), Examples of unit-LFP coherence analysis for different neurons from the same recording session. Top, unit-LFP coherence (gray shading, 95 percentile confidence bands), middle, phase spectrum (0, unit is locked to the peak of the LFP); bottom, anatomical map of spike-LFP coherence at maximal coherence frequency. Circle, putative location of the soma of the unit; cross, site used on the top plots. Note variability of localization in frequency and

anatomical location of the maximal gamma coherence of the LFP to different neurons. **(D,E)**, Spike-triggered average spectra for 2 example units. Left panels, deviation of the spike-triggered spectral power from baseline as a function of recording sites (only recording sites without artifacts are shown, y-axis) and frequency (x-axis). Middle panels, anatomical map of spike-triggered spectral power at maximal gamma frequency. Circle, putative cell body location of the unit; cross, site with maximal gamma power. Malfunctioning sites and sites with large amplitude unit spikes (gray) were excluded from the analysis to avoid contamination of gamma power by spike waveshape. Right panels, spike-triggered (time zero) spectral power at the site of maximal gamma power as a function of time lag from the spike. Note similarity in frequency and spatial profiles of the gamma range unit-LFP coherence and unit-triggered spectra. **(F-I)**, Average normalized anatomical maps for four anatomical clusters of gamma power profiles triggered by different neurons. Each cluster consists of single unit-triggered profiles with the same or closely overlapping anatomical profile (D,E middle), regardless of gamma frequency. Black lines connect the center of mass of individual unit spike-triggered profiles to the location of the neuron. Note that neuron firing is occasionally best correlated with gamma power increase located as far as 1 mm from the neuron, although most long distance couplings occur in the same cortical layer (putative layer 5, F,G, E).

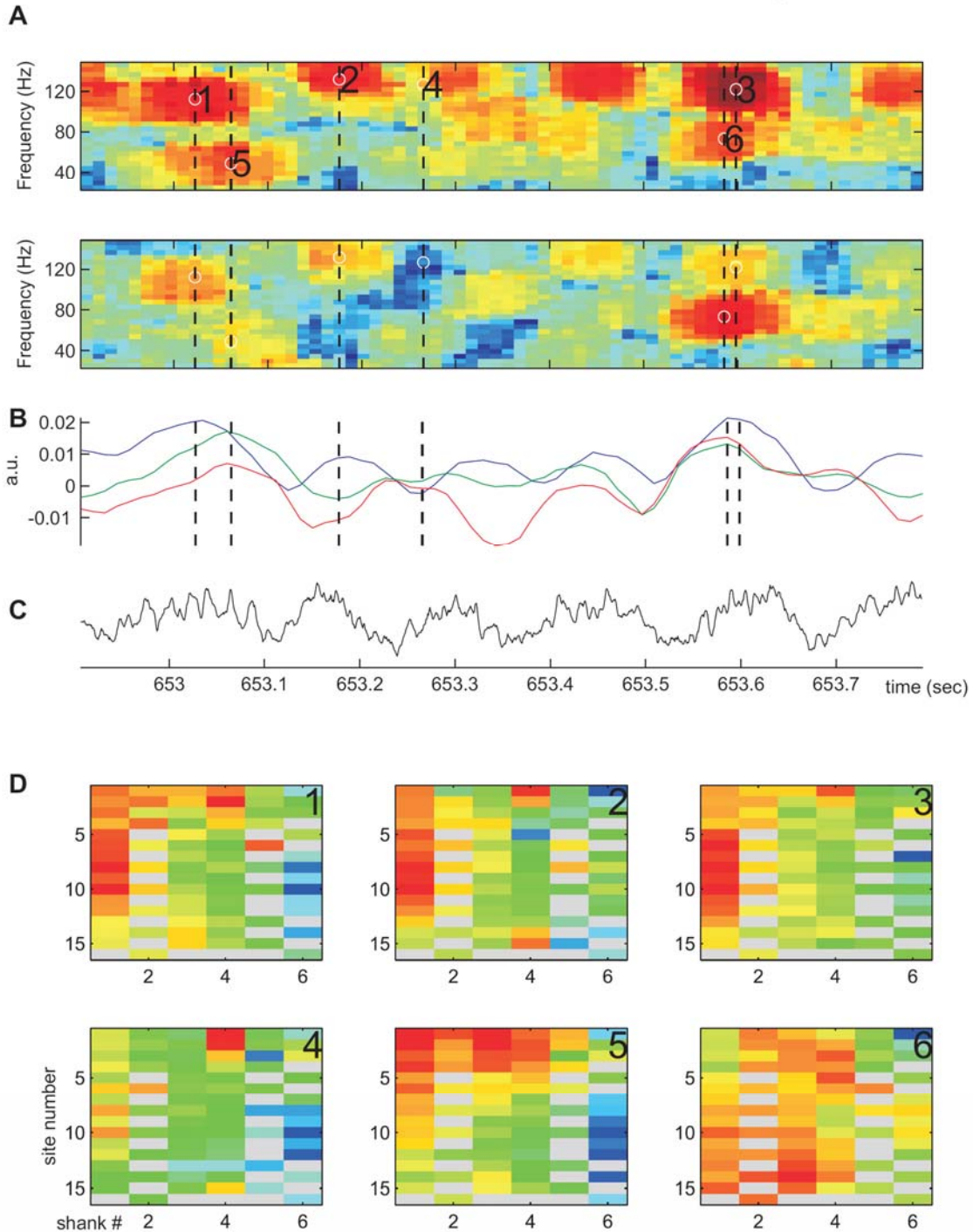


Figure S7. Fine temporal structure of the gFL score signals . (A) Sample spectrograms of whitened LFP recorded in neocortical layer 5 (A, top) and hippocampal CA1 pyramidal layer (A, bottom). Dotted lines 1-6 mark time-frequency maxima of spectral power in one of the locations. (B) Time course of the 3 gFL scores for the same time period. Blue and green traces correspond to neocortical gFLs and red trace corresponds to hippocampal gFL, whose location-frequency profiles are shown in Figure 5F, 5E and 5H, respectively. Note that times of the peaks of gFL scores closely match the

time of the peaks in the spectrograms (dotted lines 1-3,5 and 6). **(C)** LFP trace recorded in the CA1 pyramidal layer illustrating ongoing theta oscillation. **(D)** Spatial profiles of spectral power at times and frequency bins marked 1-6 in (A). Anatomical layout of recording sites as in Figure 3A. Note that spatial profiles and frequencies at peaks 1-3, 5 and 6 closely correspond to the location-frequency profiles associated with gFLs in Figure 5F, 5E and 5H, respectively. These observations illustrate that peaks in the gFL score exactly correspond to the peaks in spectral power localized in space and frequency according to the respective gFL profile. Note that event 6 corresponds to two gamma oscillations simultaneously present in the hippocampus and neocortex.

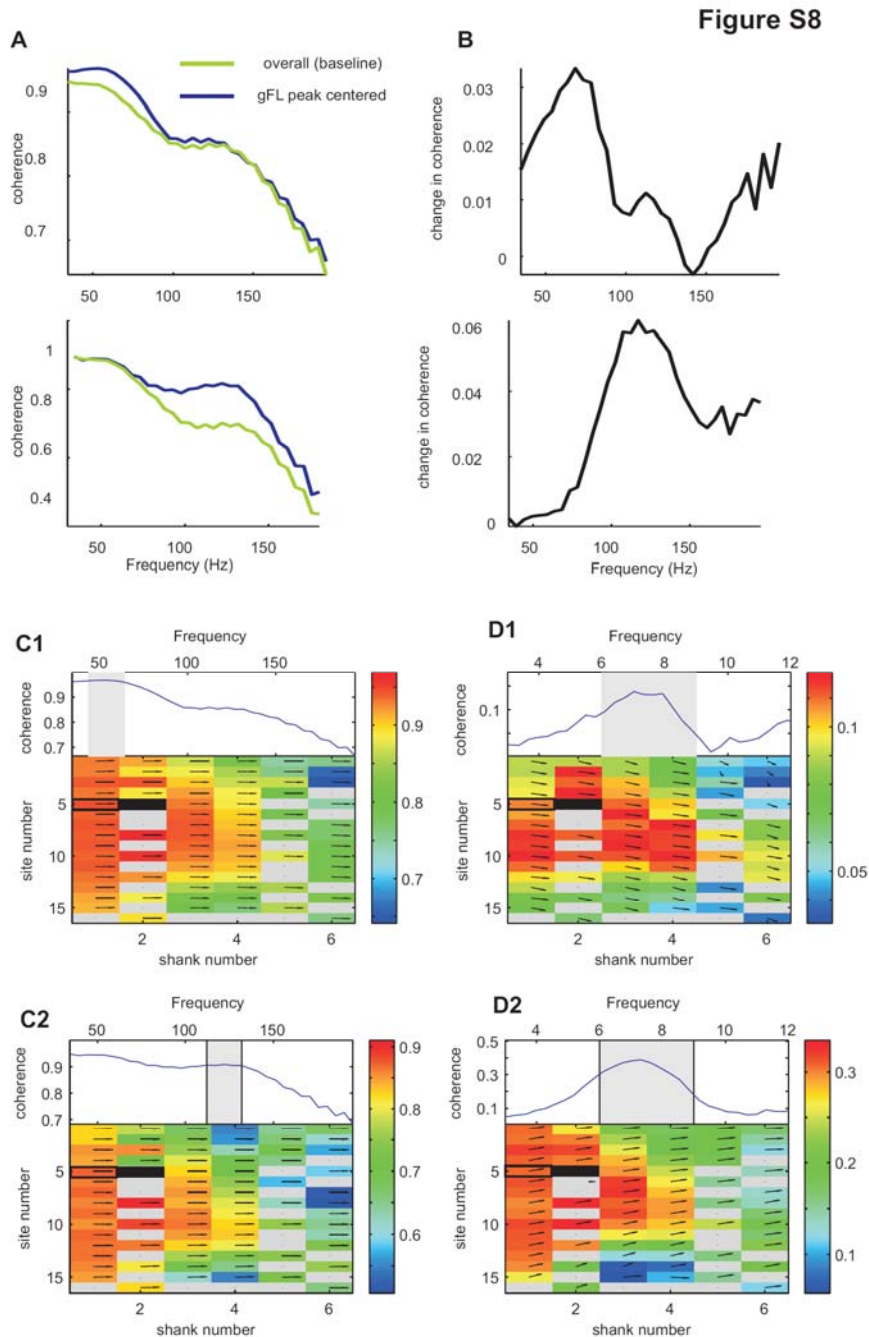


Figure S8. LFP-LFP coherence analysis. (A) Example of LFP-LFP coherence between the center of gFL (top #2 Figure 5C and bottom #4 Figure 5D) and a nearby recording site for the entire session (green, baseline) and for spectral windows confined to the time of the peaks of the respective gFL scores (blue). (B) The difference between the two coherence spectra in A. Note that peak-confined coherence of gFL score has a frequency-specific increase. (C,D) Same display as in Figure 6 J,K for the same gFLs as in A (#2 C1,D1 and #4 C2,D2, respectively). (C1,2) Bottom, spatial map of average coherence between the LFP at the site (solid rectangle) in the center of the respective gFL and other sites at the peak frequency of the gFL profile. Top trace, example coherence for one site

(open rectangle). Arrows, phase shift (zero at 3 o'clock). (D1,2) Top, coherence spectrum between theta LFP and gamma coherence between two neocortical selected sites (theta modulation of coherence). Integrated coherence within the frequency band of maximum coherence was first computed in sliding windows and the coherence between the resulting time series and hippocampal LFP was computed. Bottom, spatial map of theta modulation of coherence between the reference gFL center site and all other sites. Note that the phase shift between hippocampal LFP and neocortical gamma (arrows; 3 o'clock is zero) is different for low and high frequency gamma. This is in agreement with the gFL analysis (Figure 6I), which also showed that the fast gamma is biased to a later phase of theta than low frequency gamma.

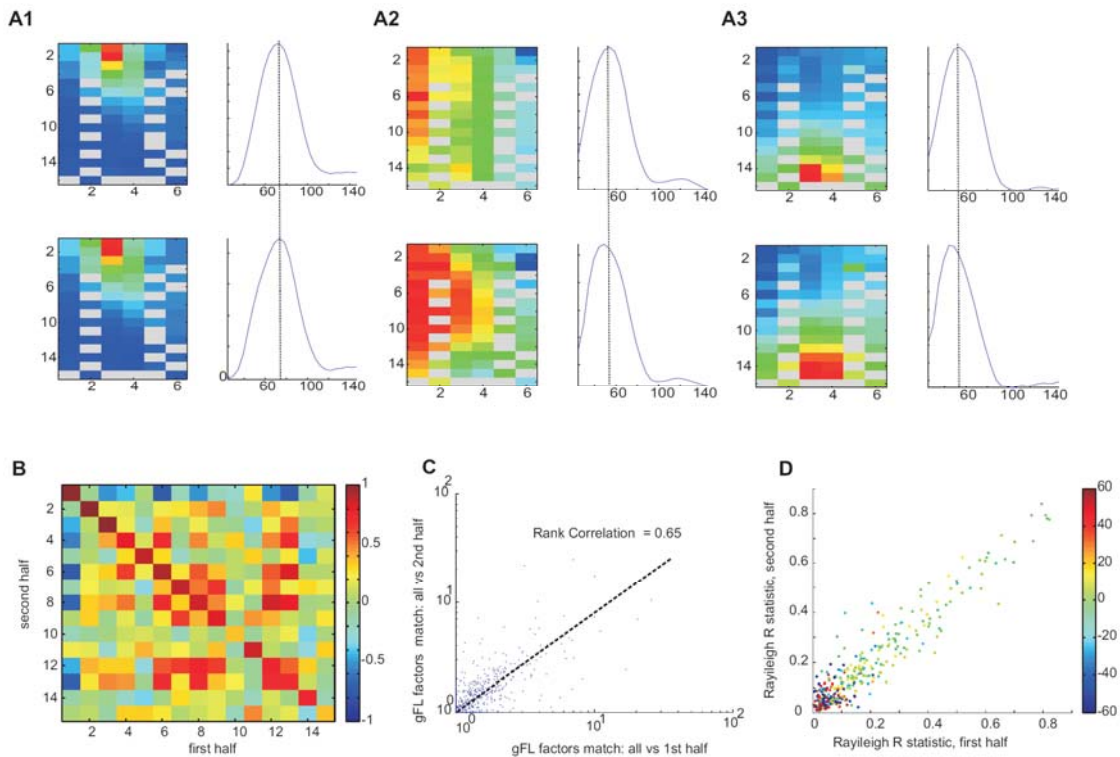


Figure S9. Stability of spatio-temporal features of neocortical gamma oscillations identified by gFL analysis. (A1-3) Spatial and frequency profiles of gFLs computed separately from the entire session (top) and first half of the session (bottom). Displays as in Figure 5. (B) Rank correlation matrix of aligned gFL factors computed from the first half and second halves of session. Note high values in the diagonal compared to off-diagonal. (C) Group data showing the correlation between gFL vector match indexes for the first and second halves. The match index was computed as the ratio of the correlation of the gFL factor in the first (second) half to the closest gFL factor derived from the second half, normalized by the correlation to the next closest gFL from the entire section. Strong correlation between the two halves demonstrates the stability of space-frequency profiles of gamma oscillations and robustness of gFL analysis. (D) Rayleigh resultant length (circular measure of concentration of the gFL peaks within the theta cycle) during the first and second halves. Color indicates the phase shift between preferred phases of

gFL peaks within the theta cycle for the two halves of the sessions. Note stability of the theta phase modulation of gFLs within session.

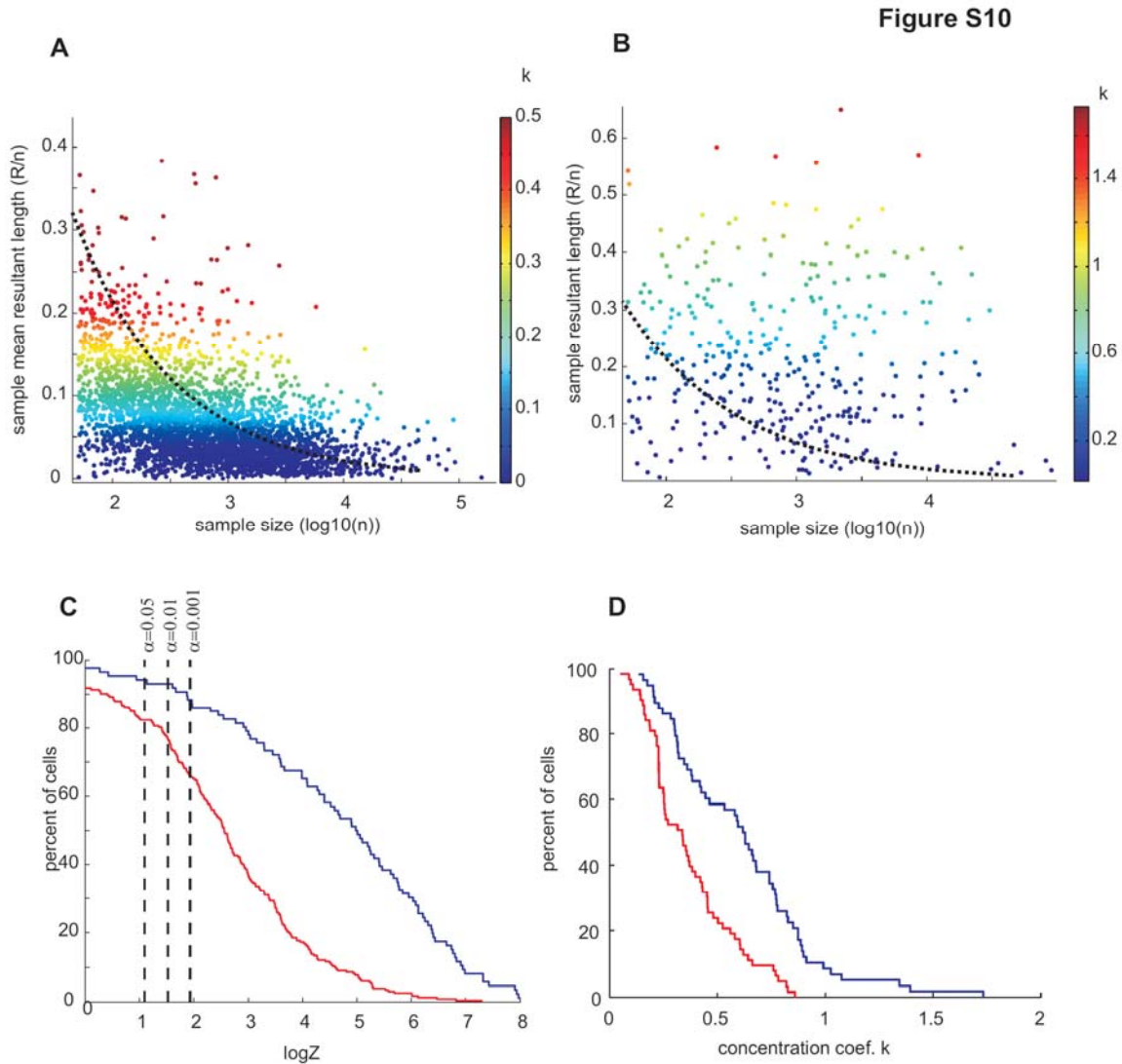


Figure S10. Hippocampal theta phase modulation of hippocampal neurons. (A,B) Theta modulation of neocortical (A) and hippocampal neurons (n=349 neurons recorded in CA1, CA3 and dentate regions combined, B). Scatter plots (each dot represents a neuron) of sample resultant length versus sample size (\log_{10} scale) with ML estimate of concentration coefficient k color coded. Note difference in color scales. Dots above the dotted line correspond to significantly (at $p < 0.01$) theta modulated neurons. Note that density of dots in $R/n - \log_{10}(n)$ space is virtually uniform in the hippocampus, in contrast to that observed in the neocortex. Most hippocampal cells are significantly modulated compared to the smaller percentage of neocortical cells. (C) Percent of neurons (y-axis) with $\log Z$ statistics greater than given (x-axis, $y = P(X > x)$). Note that putative interneurons are more likely to be significantly modulated than putative pyramidal cells. Blue, putative interneurons; red, putative pyramidal cells. Vertical dotted lines represent critical values of $\log Z$ for three levels of significance. (D) Percent of significantly

modulated neurons with concentration coefficient k greater than given (x-axis, $y = P(X > x)$). Note that in contrast to the neocortex (Figure S2C-F), hippocampal interneurons are more strongly theta-modulated than pyramidal cells. This may be due to two factors. First, hippocampal pyramidal cells exhibit network dynamics that can accelerate relative to the mean field (Geisler et al., 2007), resulting in a decrease of their concentration coefficient. Second, afferents of most hippocampal interneurons are periodic at theta frequency.

Supplemental References

Bartho, P., Hirase, H., Monconduit, L., Zugaro, M., Harris, K.D., and Buzsaki, G. (2004). Characterization of neocortical principal cells and interneurons by network interactions and extracellular features. *J. Neurophysiol.* 92, 600-608.

Bentley, J.J., Lockhart, R.A., and Stephens, M.A. The uniform and von Mises mixture distribution; with applications. 2007. Burnaby, BC, Canada, Department of Statistics and Actuarial Science, Simon Fraser University.

Ref Type: Report

Constantinidis, C., Franowicz, M.N., and Goldman-Rakic, P.S. (2001). Coding specificity in cortical microcircuits: a multiple-electrode analysis of primate prefrontal cortex. *J. Neurosci.* 21, 3646-3655.

Csicsvari, J., Henze, D.A., Jamieson, B., Harris, K.D., Sirota, A., Bartho, P., Wise, K.D., and Buzsaki, G. (2003). Massively parallel recording of unit and local field potentials with silicon-based electrodes. *J. Neurophysiol.* 90, 1314-1323.

Csicsvari, J., Hirase, H., Czurko, A., and Buzsaki, G. (1998). Reliability and state dependence of pyramidal cell-interneuron synapses in the hippocampus: an ensemble approach in the behaving rat. *Neuron* 21, 179-189.

Csicsvari, J., Hirase, H., Czurko, A., Mamiya, A., and Buzsaki, G. (1999). Oscillatory coupling of hippocampal pyramidal cells and interneurons in the behaving Rat. *J. Neurosci.* 19, 274-287.

Freeman, J.A., and Nicholson, C. (1975). Experimental optimization of current source-density technique for anuran cerebellum. *J. Neurophysiol.* 38, 369-382.

Fujisawa, S., Amarasingham, A., and Buzsaki, G. (2008). Behavior-dependent short-term assembly dynamics in the medial prefrontal cortex. *Nat. Neurosci.* 11:823-833.

Geisler, C., Robbe, D., Zugaro, M., Sirota, A., and Buzsaki, G. (2007). Hippocampal place cell assemblies are speed-controlled oscillators. *Proc. Natl. Acad. Sci. U. S. A.* 104, 8149-8154.

- Harris,K.D., Henze,D.A., Csicsvari,J., Hirase,H., and Buzsaki,G. (2000). Accuracy of tetrode spike separation as determined by simultaneous intracellular and extracellular measurements. *J. Neurophysiol.* *84*, 401-414.
- Hazan,L., Zugaro,M., and Buzsaki,G. (2006). Klusters, NeuroScope, NDManager: A free software suite for neurophysiological data processing and visualization. *J. Neurosci. Methods* *155*, 207-216.
- Henze,D.A., Borhegyi,Z., Csicsvari,J., Mamiya,A., Harris,K.D., and Buzsaki,G. (2000). Intracellular features predicted by extracellular recordings in the hippocampus in vivo. *J. Neurophysiol.* *84*, 390-400.
- Isomura,Y., Sirota,A., Ozen,S., Montgomery,S., Mizuseki,K., Henze,D.A., and Buzsaki,G. (2006). Integration and segregation of activity in entorhinal-hippocampal subregions by neocortical slow oscillations. *Neuron* *52*, 871-882.
- Jammalamadaka,S.R., and SenGupta,A. (2001). *Topics in circular statistics* World Scientific).
- Jarvis,M.R., and Mitra,P.P. (2001). Sampling properties of the spectrum and coherency of sequences of action potentials. *Neural Comput.* *13*, 717-749.
- Kayser,J., and Tenke,C.E. (2003). Optimizing PCA methodology for ERP component identification and measurement: theoretical rationale and empirical evaluation. *Clin. Neurophysiol.* *114*, 2307-2325.
- Mardia,K.V., and Jupp,P.E. (2000). *Directional statistics* John Wiley and Sons).
- Markram,H. (2006). The blue brain project. *Nat. Rev. Neurosci.* *7*, 153-160.
- Montgomery,S.M., and Buzsaki,G. (2007). Gamma oscillations dynamically couple hippocampal CA3 and CA1 regions during memory task performance. *Proc. Natl. Acad. Sci. U. S. A* *104*, 14495-14500.
- Reyment,R., and Joreskog,K.G. (1993). *Applied Factor Analysis in the Natural Sciences* Cambridge University Press).
- Schou,G. Estimation of the concentration paramter in von Mises-Fisher distributions. *Biometrika* *65*, 369-377. 1978.
- Siapas,A.G., Lubenov,E.V., and Wilson,M.A. (2005). Prefrontal phase locking to hippocampal theta oscillations. *Neuron* *46*, 141-151.
- Sirota,A., Csicsvari,J., Buhl,D., and Buzsaki,G. (2003). Communication between neocortex and hippocampus during sleep in rodents. *Proc. Natl. Acad. Sci. U. S. A* *100*, 2065-2069.

Somogyi,P., Tamas,G., Lujan,R., and Buhl,E.H. (1998). Salient features of synaptic organisation in the cerebral cortex. *Brain Res Brain Res Rev* 26, 113-35.

Thomson,D.J., and Chave,A.D. (1991). Jackknifed error estimates for spectra, coherences and transfer functions. S. Haykin, ed. Prentice Hall).

Zugaro,M.B., Monconduit,L., and Buzsaki,G. (2005). Spike phase precession persists after transient intrahippocampal perturbation. *Nat. Neurosci.* 8, 67-71.